Supporting Information

Nanocrystals in Molten Salts and Ionic Liquids: Experimental Observation of Ionic Correlations Extending beyond the Debye Length

Vladislav Kamysbayev,[†#] Vishwas Srivastava,[†#] Nicholas B. Ludwig,[†#] Olaf J. Borkiewicz,[‡] Hao Zhang,[†] Jan Ilavsky,[‡] Byeongdu Lee,[‡] Karena W. Chapman,[‡⊥] Suriyanarayanan Vaikuntanathan,[†] Dmitri V. Talapin[†§*]

[†]*Department of Chemistry and James Franck Institute, University of Chicago, Illinois, 60637, United States*

[‡]*X-ray Science Division, Advanced Photon Source, Argonne National Laboratory, Argonne, Illinois, 60439, United States*

[⊥]*Present Address: Department of Chemistry, Stony Brook University, Stony Brook, New York 11790, United States*

[§]*Center for Nanoscale Materials, Argonne National Laboratory, Argonne, Illinois, 60439, United States*

# These authors contributed equally.

*E-mail: dvtalapin@uchicago.edu

Experimental Section

Chemicals and materials

Sodium thiocyanate (NaSCN, ≥99.99 %, trace metal basis, Aldrich), Potassium thiocyanate (KSCN, ACS reagent, ≥99.0 %, Aldrich), Aluminum chloride ($AlCl_3$, 99.99 %, trace metal basis, Aldrich), Sodium chloride (NaCl, puratronic, 99.999 %, metal basis, Alfa Aesar), Potassium chloride (KCl, 99.999 %, trace metal basis, Aldrich), 1-butyl-3-methylimidazolium chloride (98 %, Strem Chemicals), 1-butyl-3-methylimidazolium tetrafluoroborate (98 %, Strem Chemicals), 1-butyl-3-methylimidazolium iodide (99 %, Aldrich), 1-butyl-3-methylimidazolium bromide (≥98.5 %, HPLC grade, Aldrich), Didodecylammonium bromide (DDAB, 98 %, Aldrich), Ammonium sulfide (40-48% in water, Aldrich), Nitrozonium tetrafluoroborate powder ($NOBF_4$, 97 % Aldrich), Tetrafluoroboric acid (HBF_4, 48 % in water, Aldrich), Oleylamine (70 %, Aldrich), octadecene (90 %, Aldrich), oleic acid (90 %, Aldrich), Tri-n-octylphosphine oxide (TOPO, 99 %, Aldrich), Formamide (99.5 %, Aldrich), Toluene (Anhydrous, 99.8 %, Aldrich), acetonitrile (Anhydrous, 99.8 %, Aldrich) Zirconium (IV) isopropoxide isopropanol complex (99.9 %, Aldrich), Zirconium (IV) chloride (sublimed grade, >99.95 %, Strem Chemicals), Indium (III) chloride ($InCl_3$, anhydrous, 99.99 %, Puratrem),) tris(trimethylsilyl) arsine ($(TMS)_3As$) was prepared as detailed in the literature[1], tri-n-octylphosphine (TOP, 97 %, Strem Chemicals), Tri(trimethylsilyl) phosphine ($(TMS)_3P$, 98 %, Strem Chemicals), CdO (≥99.99 %, Aldrich), Se (99.99 %, 100 mesh, Aldrich), Iron (0) pentacarbonyl (>99.99 %, Aldrich), Platinum (II) acetylacetonate (97 %, Aldrich). Oleylamine, octadecene and formamide were dried under vacuum before use. $AlCl_3$ was purified by sublimation in a nitrogen filled glovebox prior to use.

Characterization Techniques

X-ray photoelectron spectroscopy (XPS). InAs NCs were recovered from $BMIM^+I^-$ IL by dissolving the matrix in CH_3CN. The recovered particles were drop-casted onto a Si wafer inside a glovebox and quickly transferred to XPS chamber with minimal exposure to air. XPS analysis was performed on a Kratos Axis Nova spectrometer using monochromatic Al K_α source (1486.6 eV). In 3d high-resolution spectra were collected using an analysis area of 0.3X0.7 mm^2 and 20 eV pass energy with the step size of 0.1 eV. Charge neutralization was performed using a co-axial, low energy (≈0.1 eV) electron flood source to avoid shifts in the recovered binding energy.

The spectra were fit in CasaXPS using Shirley background.

^{1}H NMR of CdSe NCs. Oleic acid (OA) capped CdSe NCs in hexane were dried thoroughly and redispersed in d^8-toluene with the concentration of 25 mg/ml. To test the existence of OA ligands on CdSe NC surface after their phase transfer to $BMIM^+Cl^-$ IL, we recovered the organic ligands (if any) by digesting CdSe to avoid interferences from imidazolium ring. In brief, DI water was

used to dissolve IL matrix. The NC precipitates were rinsed with water several times to completely remove IL residue. Afterward, CdSe NCs were dissolved in half concentrated aqua regia using standard procedures.[2] The organic ligands (if any) were then extracted with diethyl either, dried under vacuum and dissolved in d^8-toluene for NMR study.

Small Angle X-ray Scattering (SAXS) analysis

SAXS modelling

The SAXS curves were analyzed by fitting to a quantitative model in Igor Pro using the Irena package (available at https://usaxs.xray.aps.anl.gov/software/irenafrom the APS).[3] Structure factor free scattering curves (*S(q)~1*) (after appropriate background subtraction) were fitted with the model independent maximum entropy approach. Based on TEM data, the particles' form factor was assumed to be spherical with the aspect ratio of 1.

Modelling of dispersions of interacting particles ($S(q)\neq1$) was performed in Modelling II module in Irena package. The primary particles (population 1) were modelled using the Gaussian size distribution with the hard sphere structure factor. The secondary structures (population 2) were modelled using the Unified Fit level.[4] To further extract approximate *S(q)*: (i) the interparticle interactions were "switched off" (dilute limit) in the appropriate model and population 2 was removed as well, thus rendering $|F(q)|^2$ of the primary particles; (ii) background corrected experimental intensity was normalized by the form factor from (i), $S(q) = I(q)/|F(q)|^2$.

PDF-SAS analysis

We use the same definition of the PDF-SAS as for the atomic PDF (see eq. 4 below):

$$PDF - SAS = \frac{2}{\pi}\int_{q_{\min}}^{q_{\max}} dqq(S(q)-1)\sin(qr) \quad (1)$$

Here *S(q)* is the structure factor extracted from the corresponding SAXS intensity curves (as in section 2.2), q_{min} = 0.02 Å^{-1} and q_{max} = 0.18 Å^{-1} for CdSe/CdS core-shell NCs.

Atomic Pair Distribution Function (PDF) analysis

Atomic PDF extraction

Conversion to the respective structure factor and pair distribution function was performed in PDFGetX2.[5] A typical procedure for the extraction of the structure factor and PDF was as following and it is similar to that of Zobel *et al*.:[6]

1. Molten salt without NCs in 1.1 mm outer diameter (0.1 mm thickness) borosilicate capillary was used as a background to subtract the scattering corresponding to bulk liquid, glass and experimental set-up from the dispersion of NCs in the same molten salt formulation (empty glass capillary was used as a background for pure molten salt and NCs in dry powdered state).
2. The background subtracted scattering intensity was corrected for Compton scattering and detector effects ($I_{corrected}$) and further converted to the respective structure factor ($S(q)$) using the atomic form factors (f) of the known elemental composition of NCs (or elemental composition of salt or ILs in case of the structure factor for bulk liquid):

$$S(q) = 1 + \frac{I_{corrected} - \langle f^2 \rangle}{\langle f \rangle^2} \tag{2}$$

   The reduced structure factor can be further calculated as following:

$$RSF = q\left(S(q) - 1\right) \tag{3}$$

3. The PDF function was extracted by the Fourier transformation of the respective reduced structure factor (eq.3) using the transferred momentum range ($q = \frac{4\pi \sin(2\theta/2)}{\lambda}$ where λ is X-ray wavelength and 2θ is the scattering angle) from q_{min}=0.6 Å^{-1} to q_{max}=14-20 Å^{-1} in case of solutions of NCs in molten salt and ILs and 20-24 Å^{-1} in case of NC powders and bulk liquids:

$$G(r) = \frac{2}{\pi} \int_{q_{\min}}^{q_{\max}} dq q (S(q) - 1) \sin(qr) \tag{4}$$

   The chosen q_{min} of 0.6 Å^{-1} guarantees that there is minimum contribution from the SAXS region of NCs and at the same time it should capture all FSDPs of the restructured and bulk molten salts and ILs.
4. The double differential PDFs (dd-PDF) for NCs in molten salts and ILs were obtained using PDFGui.[5] The differential PDF (d-PDF) of NCs in molten salt has almost no contribution from the oscillatory component of the restructured solvent at r>20 Å. Hence the region of the d-PDF at r>20 Å was modelled using the refined crystal structure of NCs only to render the scaling factor for the NC phase. The refined parameters such as lattice constants and atomic displacement factors were extracted from modelling of NCs powder without any solvent. The particle diameter was not refined and determined independently from SAXS size distributions and TEM data. The obtained parameters corresponding to

the respective NC phase (scaling factor, lattice constant, atomic displacement factors, diameter) were fixed and the model was propagated into the region of r<20 Å where there is significant contribution from the oscillatory component of the restructured solvent. The resultant difference curve (residue) is the dd-PDF free of atomic correlations corresponding to bulk liquid and distances within individual NCs.

Atomic PDF fitting

Intermediate range order (IRO) component in dd-PDF of the restructured and bulk molten salt was fit with the exponentially damped sinusoidal curve:

$$G_{IRO}(r) = Acos\left(2\pi r/\lambda - \varphi\right)e^{-r/l_d} \quad (5)$$

Where l_d is the decay length of layering, λ is the wavelength fixed for the same type of the ion-pair (3.3 Å for K^+ - SCN^- and 4.0 Å for $BMIM^+$ - Cl^-), φ is the phase and A is the amplitude.

Relation between $G_{IRO}(r)$ and $RSF(q)$

The Fourier transform of eq.5 yields the following reduced structure factor (normalized by the amplitude of G_{IRO}):

$$\frac{RSF}{A} = \frac{q(S(q)-1)}{A} = q\,\frac{(q^2-(2\pi/\lambda)^2+(1/l_d)^2)cos(\varphi)+2(2\pi/\lambda l_d)sin(\varphi)}{(q^2-(2\pi/\lambda)^2)^2+(1/l_d)^4+2(q^2+(2\pi/\lambda)^2)(1/l_d)^2} \quad (6)$$

From eq. 6 it is evident that the peak position of RSF(q) (which as defined as the first sharp diffraction peak, FSDP) is a complex function of the phase and decay length of G_{IRO}. Figure S13 further illustrates this dependence for the experimentally relevant values of λ, φ and l_d.

Molecular Dynamics Simulations

Model

Nanoparticles of CdSe, InP, and chemically inert types were implemented by setting short-range interactions equivalent to those of C2 carbons in the CLDP force field and including appropriate partial charges.[7, 8] Mixing the partial charges from a crystal model with the CLDP force field is necessarily approximate, but we expect it to be a reasonable approximation – and agreement between the simulation and experimental results bears out that expectation. The interatomic distances in the nanoparticle solutes were rigidly fixed. Our choice to model the short-range interaction in such an approximate way was informed by simulation work on ionic liquid interactions with Au electrodes where the Au short-range interactions were set as graphite carbons.[9] The most important factor by far appears to be the charge of the surface, with the short-range interactions providing only a perturbation. Since most of the ion specific interactions

between the NC and the solvent is due to the Coulomb interaction, setting the charge of the NC to zero is effectively the same as making it chemically inert. And indeed, we observed that the structuring of the IL did not occur when the Coulomb interaction between nanoparticle and solvent was set to zero. Though not meant to be physically meaningful, this test confirms that the short-range interactions and exclusion volume due to the nanoparticle is not responsible for the restructuring of the IL.

Simulations were run at constant temperature and pressure with a temperature of 400K using the Nose-Hoover thermostat and a pressure of 1 bar using the Nose-Hoover barostat with coupling parameters of 500 fs and 1000 fs respectively. In runs with nanoparticles, the nanoparticles were allowed to rotate freely and were subject to a Langevin thermostatting at 400K.

Bulk simulations consisted of 480 $BMIM^+$ and 480 Cl^- ions. Simulations with nanoparticles consisted of two sets. In the first set, nanoparticles were cubic with sides approximately 3 nm in length. The nanoparticles were cut such that for CdSe (InP) there were three Cd (In) coated facets and three Se (P) coated facets. All facets were (100). For these simulations, 3630 $BMIM^+$ and 3630 Cl^- ions were used, leading to a cubic periodic box of roughly 10.5 nm in length. Larger simulations with 3 nm nanoparticles and box sizes up to 20 nm in length were used to confirm finite size effects were not an issue for the 10.5 nm box size.

Analysis

Radial distribution functions for all ion pairs were extracted from simulation trajectories. These were convoluted with appropriate atomic form factors for comparison with experiment.[10-12] Atomic form factors were approximated using sums of four Gaussians, which is a good approximation for small q.[13] The surface-induced correlations were also measured by computing the probability of observing the various fluid atom types in front of each surface of the nanoparticle as a function of the distance along surface normal. Similar post-processing with atomic form factors was required for comparison with experiment.

For comparison with experimental restructured reduced structure factors, the radial distribution functions of ion pairs were also extracted from solvent systems including nanoparticles. In these RSFs, crystal-crystal (Cd-Cd, Cd-Se, *etc*.) correlations were excluded from sums over all particle pairs, as otherwise, the crystal-crystal contributions dominate the less-ordered liquid-liquid and crystal-liquid contributions.

Estimation of the free energy of interaction for NCs in molten salt

Van der Waals potential

The Van der Waals (VdW) attraction V_{VdW} between CdSe/CdS NCs in NaSCN/KSCN molten salt can be evaluated using the Lifshitz theory. Since the distances of interest are on the order of a few nanometers, the retardation effects due to the finite speed of light can be ignored. The general expression for VdW potential between the two spheres of radius *R* separated by a distance *l* at the point of the closest approach:[14]

$$V_{VdW}(l) = -\frac{A}{6}\left(\frac{2R^2}{(4R+l)l} + \frac{2R^2}{(2R+D)^2} + \ln\left(\frac{(4R+l)l}{(2R+l)^2}\right)\right) \tag{7}$$

Where *A* is a Hamaker coefficient defined by the medium's and interacting particles' dielectric functions:

$$A = \frac{3}{2}k_b T \sum_{q=1}^{\infty} \frac{1}{q^3} \sum_{n=0}^{\infty}{}' \left[\Delta(i\omega_n)\right]^{2q} \tag{8}$$

$$\Delta(i\omega_n) = \frac{\varepsilon_1(i\omega_n) - \varepsilon_3(i\omega_n)}{\varepsilon_1(i\omega_n) + \varepsilon_3(i\omega_n)} \tag{9}$$

Here T is temperature (=473 K in case of NaSCN/KSCN molten salt) and k_b is the Boltzmann constant; ε_1 and ε_3 are the complex dielectric functions of particles (MXenes) and medium (liquid metal) respectively evaluated at imaginary Matsubara frequencies, $\omega_n = n \cdot 2\pi k_b T / \hbar$. The subscript (') in the second sum in eq. 8 indicates that the zero frequency (*n=0*) term has contribution of ½. However, since molten salts are infinitely polarizable media, the zero frequency term (equivalent to the electrostatic interaction) is screened as $e^{-\frac{l}{l_d}}$.[14] Hence, we can ignore the *n=0* term contribution to the Hamaker coefficient in eq. 8.

Here we approximate the dielectric functions of CdSe/CdS core-shell NC and NaSCN/KSCN molten salt as CdS and KCl respectively. Since complex dielectric functions at 473K (excluding the zero frequency term) are evaluated at integral multiples of $\omega_1 = 3.887 \cdot 10^{14} rad/s$, the spectral parameters in the near infrared and UV-visible ranges are of interest. It is common to approximate ε_1 and ε_3 using one UV and one IR relaxation terms:[15]

$$\varepsilon(i\omega_n) = 1 + \frac{C_{UV}}{1 + \frac{\omega_n^2}{\omega_{UV}^2}} + \frac{C_{IR}}{1 + \frac{\omega_n^2}{\omega_{IR}^2}} \tag{10}$$

Parameters for ε_1 of CdS

ω_{UV} (rad/s)	C_{UV}	ω_{IR} (rad/s)	C_{IR}
$6.92*10^{15}$	4.114	$4.6*10^{13}$	4.86

Parameters for ε_3 of KCl

ω_{UV} (rad/s)	C_{UV}	ω_{IR} (rad/s)	C_{IR}
$1.58*10^{16}$	1.17	$2.7*10^{13}$	2.23

The numerical calculation using eq. 8 with q_{max} = 30 and n_{max} = 20000 results in $A_{CdS/KCl/CdS}$ = 22.2 zJ.

The dielectric function for Pt NCs (R = 2 nm) can be represented with the familiar Drude free-electron model whose parameters are readily available in the literature:[16]

$$\varepsilon_1(i\omega_n) = 1 + \frac{\omega_{p1}^2}{\omega_n^2 + \gamma_1\omega_n} \tag{11}$$

Parameters for ε_1 of Pt

ω_{p1}(eV)	γ_1 (meV)
5.156	69.32

The numerical calculation using eq. 8 with q_{max} = 30 and n_{max} = 20000 results in $A_{Pt/KCl/Pt}$ = 71.9 zJ.

Oscillatory potential

The oscillatory potential between CdSe/CdS NCs interacting through NaSCN/KSCN (approximated as KCl) molten salt V_{ocs} is evaluated using the continuum Ginsburg-Landau model under Derjaguin ($l << R$) approximation detailed in reference 11 of the main text:

$$V_{osc}(l) = \pi R F_0 q_0^{-1} \mathrm{e}^{-\frac{l}{l_d}} \left(\cos(q_0 l + \varphi) + \frac{l_d}{R} \right) \tag{12}$$

Here R is the radius of a NC, l is the interparticle separation, l_d = 0.496 nm is the decay length of layering (as in eq. 5), q_o = 15.373 nm^{-1} is the preferred wavenumber of layering, $\varphi = tan^{-1}\left(\frac{1}{l_d q_0}\right) = 7.472$ is the phase and F_0 is the energy scale. For KCl interacting with the Cd-terminated (100) facet of CdS NCs the energy scale can be estimated as $F_0 \sim \frac{\psi_0 l_d k_b T}{\sigma^3} =$

$\frac{1*0.496*1.38*10^{-23}*473}{0.31^3} = 108.7\ zJ/nm^2$ (σ is related to the size of ions in the melt, 3.1 Å for KCl, ψ_0 is the ion density at the NC surface fixed by the strong binding affinity).

The purely repulsive contribution in eq. 12 scales as 1/R suggesting that larger particles are more likely to get kinetically trapped by large oscillatory barrier. This is likely the case for CdSe/CdS NCs with R = 6.45 nm in NaSCN/KSCN melt for which the experimentally observed interparticle distance of ~5 Å in "worm-like" aggregates is close to the computed secondary minimum at ~5 Å (Figure S5).

For smaller particles (e.g 4 nm Pt NCs) the Derjaguin is no longer applicable. Since majority of NCs are faceted, it is reasonable to approximate shape of Pt NCs by a spheroidal shape. Here we represent Pt NCs as a truncated icosidodecahedron. The total oscillatory potential is then a linear combination of the oscillatory potentials between one pair of parallel facets (decagons) and 5 pairs of tilted facets (squares and hexagons):

$$V_{osc}(l) = Area_{decagon} V_{\parallel}(l) + 5a\frac{1}{2\sin(\theta_{4,10})}\int_{l}^{l+2a\sin(\theta_{4,10})} dz\left[V_{\parallel}(z) + V_{tilt}(z, 2\theta_{4,10})\right] \quad (13)$$
$$+5\frac{1}{2\sin(\theta_{6,10})}\int_{l}^{l+4a\sin(\theta_{6,10})\cos(\pi/6)} dz\left[V_{\parallel}(z) + V_{tilt}(z, 2\theta_{6,10})\right] w(z-l)$$

$$V_{\parallel}(z) = -\frac{F_0}{2} e^{-\frac{z}{l_d}} \cos(q_0 z + \varphi) \quad (14)$$
$$V_{tilt}(z,\theta) = \frac{F_0}{l_d q_0} e^{-\frac{z}{l_d}} \theta^2$$
$$w(z-l) = a + (z-l)\frac{\tan(\pi/6)}{\sin(\theta_{6,10})}, (z-l) \le 2a\sin(\theta_{6,10})\cos(\pi/6)$$
$$w(z-l) = a(1+4\sin(\pi/6)) - (z-l), (z-l) > 2a\sin(\theta_{6,10})\cos(\pi/6)$$

Here F_0, q_0, l_d and φ have the same values as for the spherical geometry mentioned above; $\theta_{4,10}$ is the dihedral angle between decagon and square (142.62°); $\theta_{6,10}$ is the dihedral angle between decagon and hexagon (148.28°); and $a = R\sqrt[3]{\frac{4\pi}{3(95+50\sqrt{5})}} = 0.5452\ nm$ corresponds to the edge length of a truncated icosidodecahedron for a R = 2 nm Pt NC.

Supporting Tables and Figures

Table S1. Summary of the experimental details of the ionic solutions of NCs used in this study.

Ionic solvent	NCs	m.p.	Preparation temperature	Temperature during in-situ X-ray measurement
$AlCl_3$/NaCl/KCl ($AlCl_3$/$AlCl_4^-$ eutectic)	Pt	90°C	150°C	140°C
NaSCN/KSCN (eutectic)	Pt, Pd, CdSe/CdS core-shell, InP, ZrO_2	140°C	250°C	200°C
$BMIM^+Cl^-$	Pt, CdSe, InP, InAs	73°C	100°C	100°C
$BMIM^+Br^-$	CdSe	65°C	100°C	100°C
$BMIM^+I^-$	CdSe, InAs	<R.T.	50°C	50°C

Table S2. Summary of the sizing parameters extracted for CdSe/CdS core-shell QDs. The average sizes were calculated from the size distributions extracted from the fits of the corresponding SAXS I(q) curves. The center-to-center distances were measured from the PDF-SAS curves in Figure S4. Interparticle distances are approximated as the difference between the first and second columns.

Sample	Center-to-center distance [Å]	Average Size [Å]	Interparticle distance [Å]
QDs in NaSCN/KSCN melt @ 250°C	133.4±9.8	128.7±10.9	~5
Bare QDs after annealing @ 250°C	131.6±12.8	131.0±14.4	~0
Bare QDs @ RT	134.2±10.0	131.0±10.9	~3

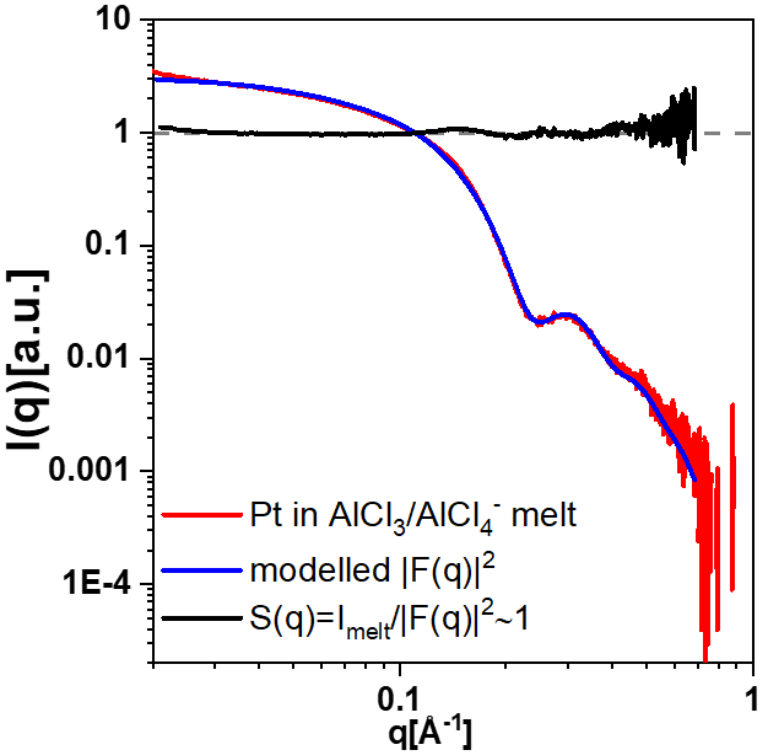

Figure S1. SAXS curves, modelled form factors, $|F(q)|^2$, and evaluated structure factors, *S(q)*, for Pt NCs in molten $AlCl_3/AlCl_4^-$. *S(q)* was extracted by dividing scattering intensities by the corresponding modelled form factor of Pt NCs in $AlCl_3/AlCl_4^-$ (more details in section 2.2 of SAXS analysis).

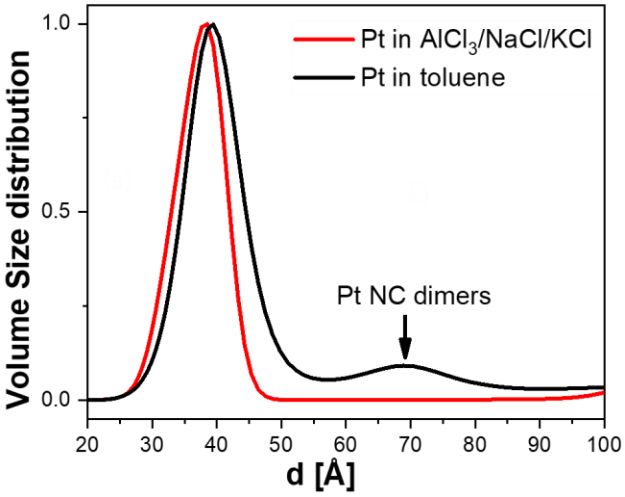

Figure S2. Comparison of the size distributions of Pt NCs dispersed in toluene and $AlCl_3/AlCl_4^-$. Some Pt NCs in toluene were not completely separated and formed dimer structures. These dimers were absent in case of Pt NCs in $AlCl_3/AlCl_4^-$ melt.

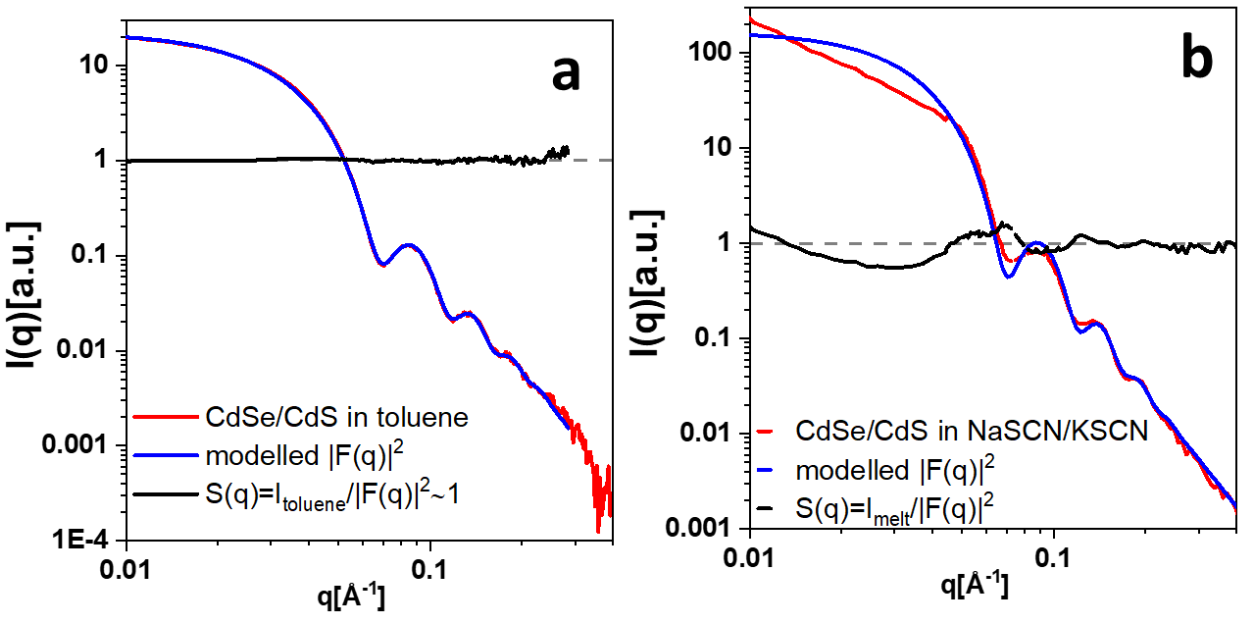

Figure S3. SAXS curves, modelled form factors, $|F(q)|^2$, and evaluated structure factors, $S(q)$, for CdSe/CdS core-shell NCs in: (a) toluene; (b) NaSCN/KSCN melt. S(q) of CdSe/CdS NCs in (b) is non-constant across the measured q range.

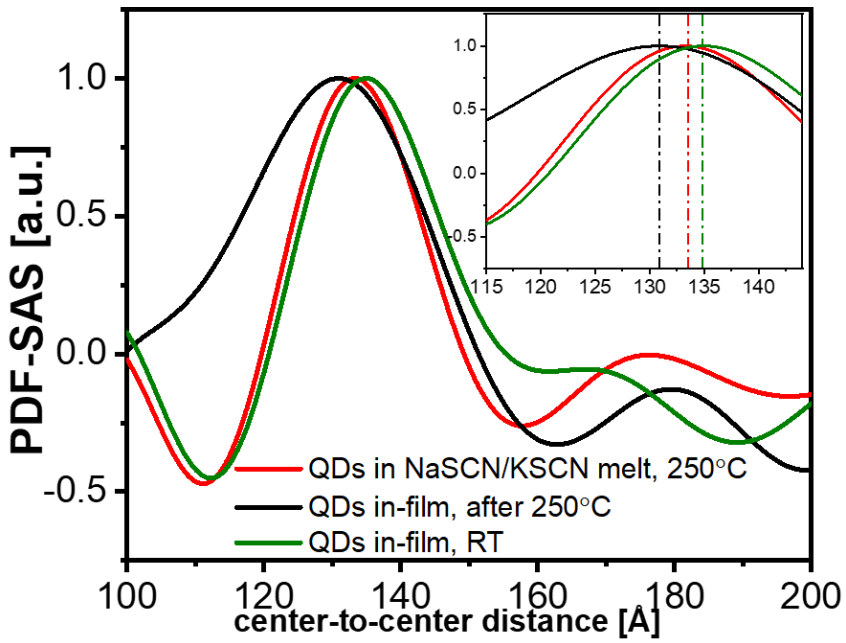

Figure S4. PDF-SAS functions calculated from the corresponding structure factors of CdSe/CdS QDs in NaSCN/KSCN melt and the same bare QDs present as a spin-cast film at RT and after additional annealing the film at 250°C for 24h.

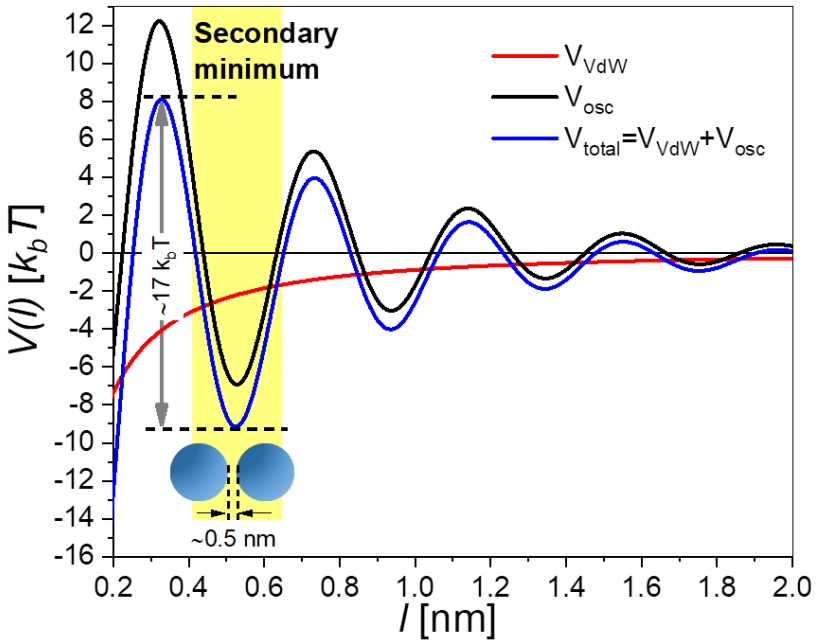

Figure S5. The free energy of interaction for CdSe/CdS NCs (approximated as CdS) in NaSCN/KSCN (approximated as KCl) molten salt at 473 K. The VdW potential is computed using the non-retarded Lifshitz theory (eq. 7). The oscillatory potential is computed using the Ginsburg-Landau model under Derjaguin approximation (eq. 12). The estimated location of the secondary attractive minimum at ~ 5 Å is in good agreement with the experimentally observed interparticle distance of ~ 5 Å in NaSCN/KSCN melt. CdSe/CdS NCs, kinetically trapped in this potential well, have to surmount a potential barrier of ~17 k_bT before the Van der Waals attraction takes over.

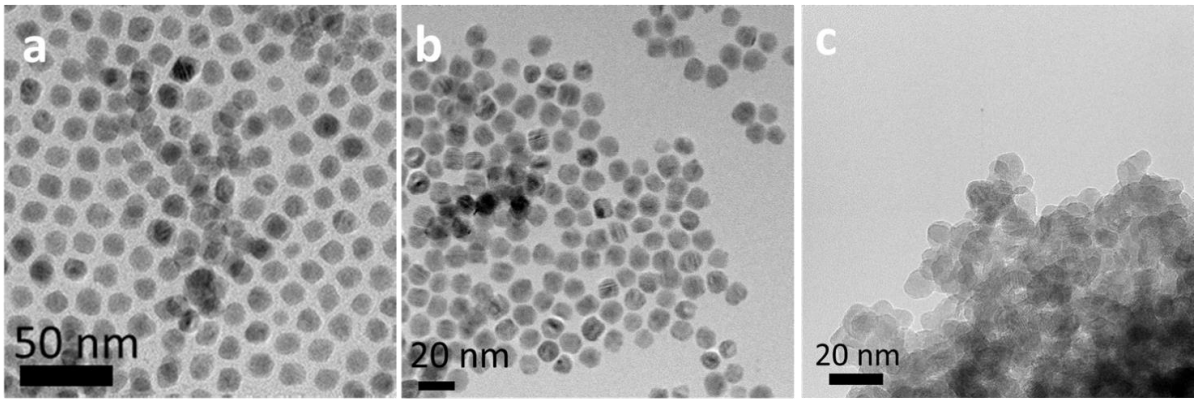

Figure S6. (a) TEM image of the initial CdSe/CdS NCs capped with organic ligands; (b) TEM image of CdSe/CdS NCs recovered after processing NCs in molten NaSCN/KSCN eutectic at 250°C for 24h. (c) TEM image of CdSe/CdS NCs recovered after annealing the bare NCs as a spin-cast film at 250°C for 24h.

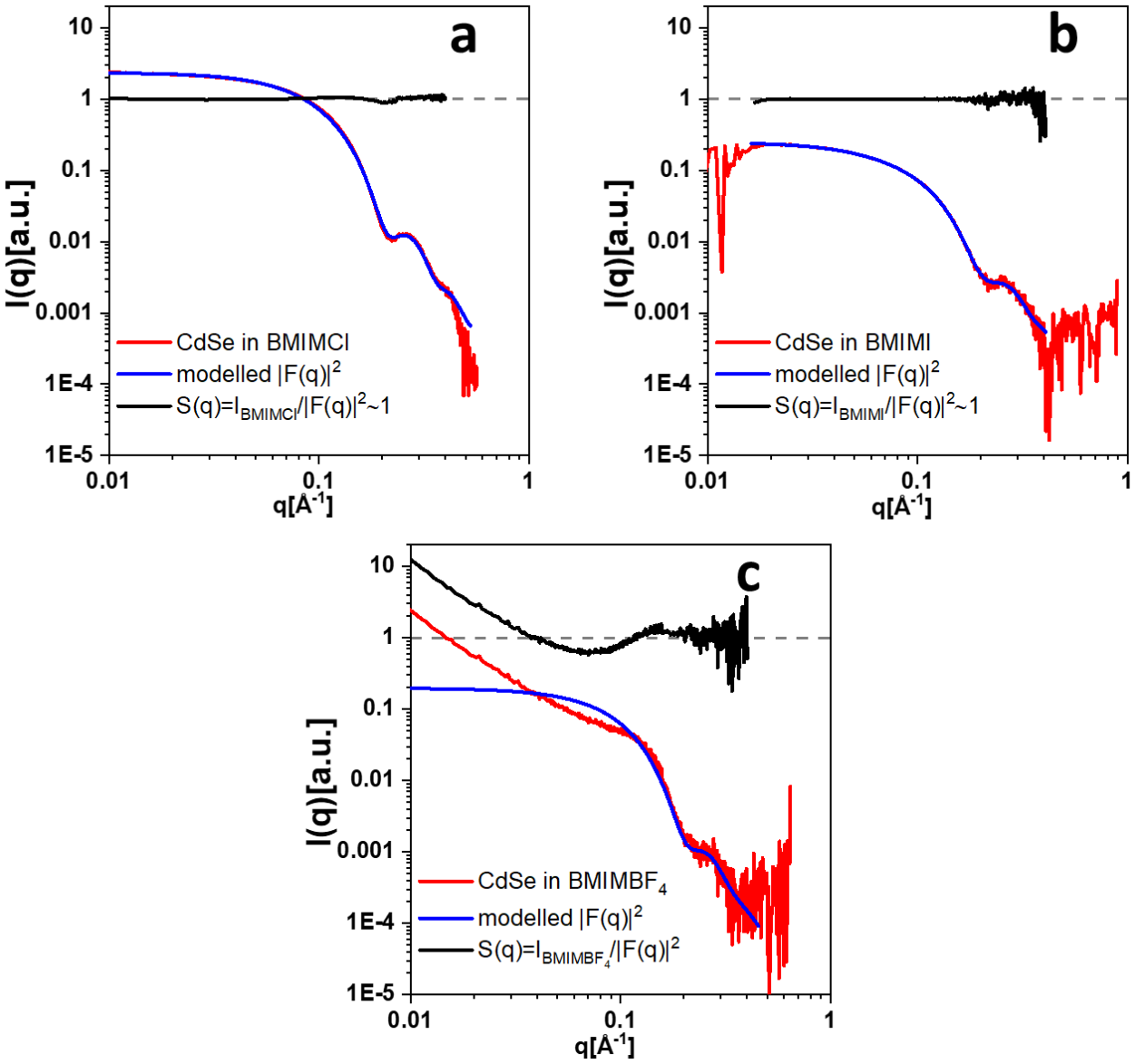

Figure S7. SAXS curves, modelled form factors, $|F(q)|^2$, and evaluated structure factors, *S(q)*, for CdSe NCs in: (a) $BMIM^+Cl^-$ IL; (b) $BMIM^+I^-$ IL; and (c) $BMIM^+BF_4^-$ IL. *S(q)* of CdSe NCs in (a) and (b) does not change across the measured q range (remains ~1). *S(q)* of CdSe in (c) is non-constant across the same q range and rises at $q<1/R_g$ (R_g=1.7 nm) suggesting presence of aggregates.

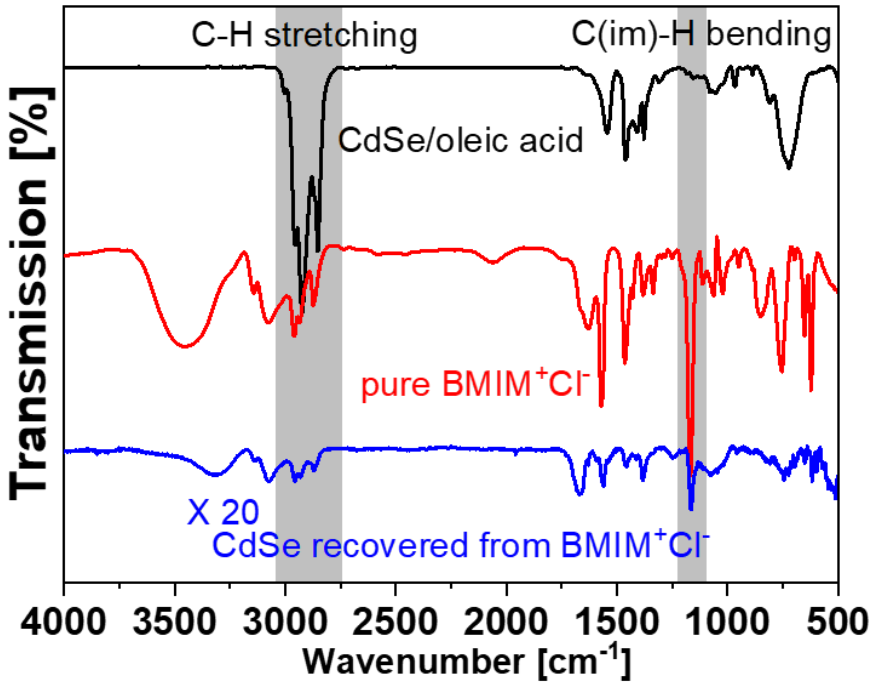

Figure S8. FTIR spectra for CdSe NCs capped with oleic acid and recovered from the stable colloidal solution in $BMIM^+Cl^-$. The spectrum of pure $BMIM^+Cl^-$ is shown for reference. The sharp peak at ~1168 cm^{-1} corresponds to the in-plane bending vibration of C-H bond of imidazolium (Im) ring.[17] This peak is absent in case of CdSe NCs capped with oleic acid.

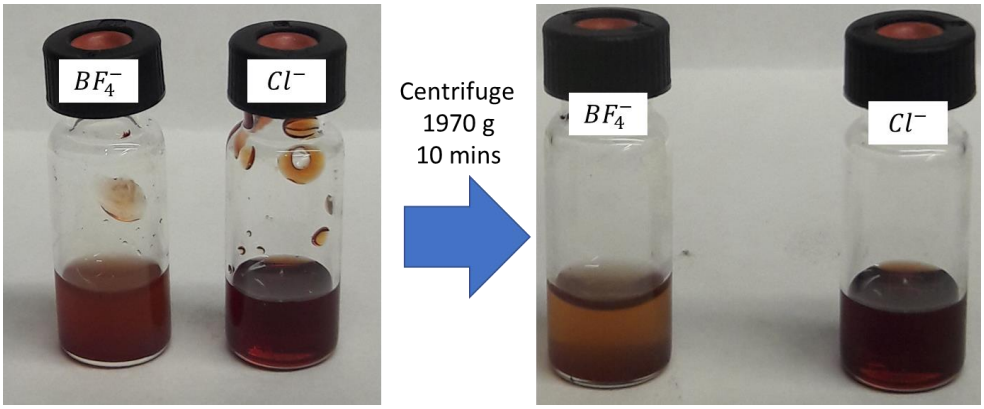

Figure S9. Photographs of CdSe NCs in $BMIM^+BF_4^-$ and $BMIM^+Cl^-$ ILs. CdSe NCs in $BMIM^+BF_4^-$ IL form a cloudy solution where NCs precipitate after centrifuging the vial at 1970 g for 10 mins. CdSe NCs in $BMIM^+Cl^-$ remain colloidally stable after 1970 g, 10 mins centrifugation.

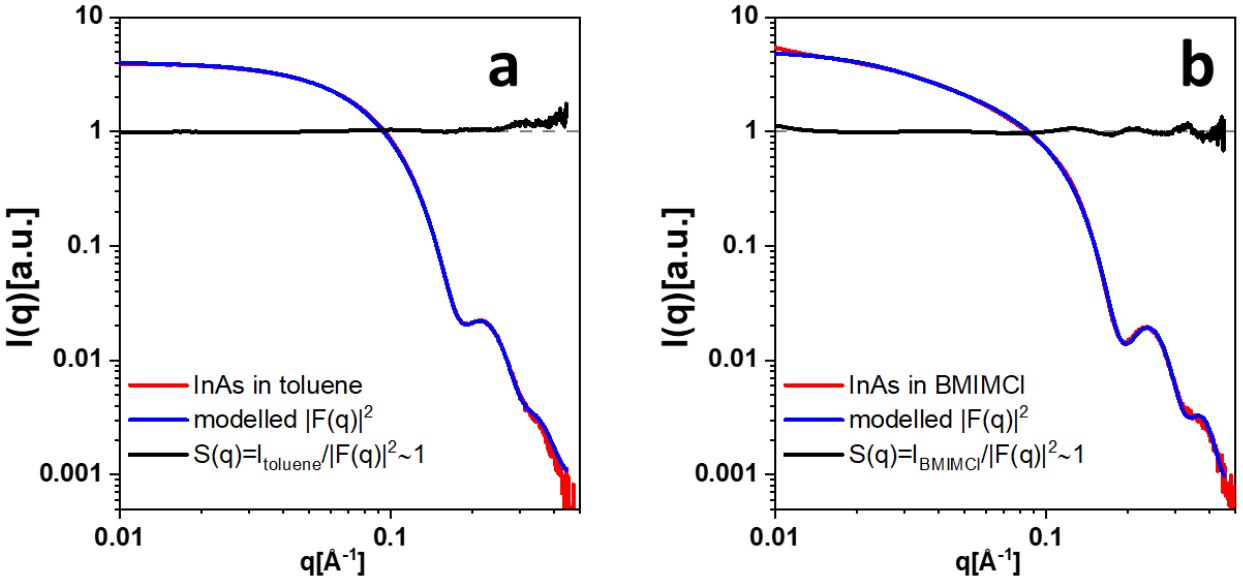

Figure S10. SAXS curves, modelled form factors, $|F(q)|^2$, and evaluated structure factors, *S(q)*, for InAs NCs in: (a) toluene; (b) $BMIM^+Cl^-$ IL. In both cases the *S(q)* remains constant ~1 across the measured q range.

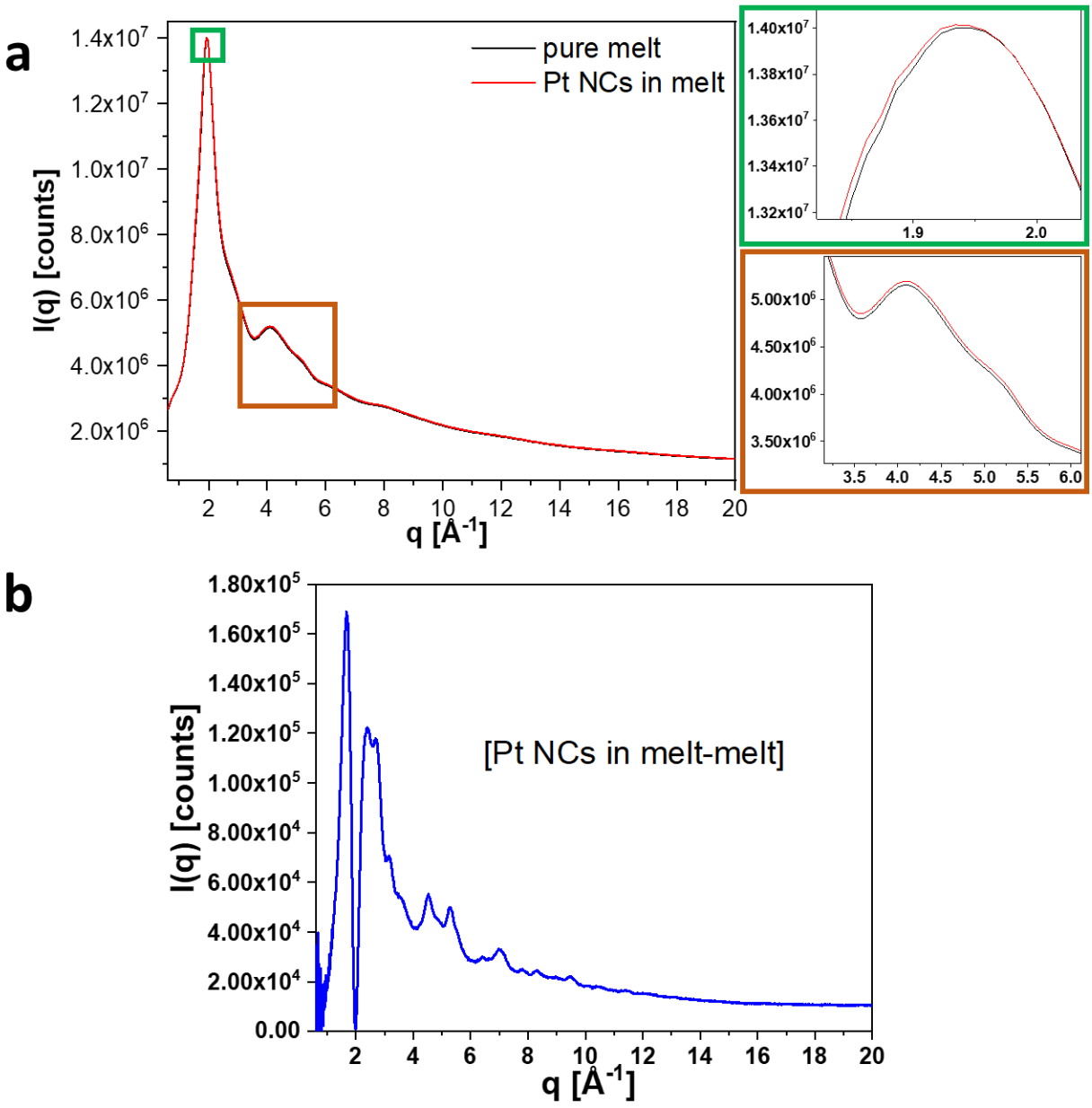

Figure S11. (a) Comparison of I(q) for pure melt with I(q) of Pt NCs dispersed in the same melt. (b) The difference curve with a new FSDP appearing at ~1.7 $Å^{-1}$ due to the interaction of ions in the melt with the NCs' surfaces. In the case of Pt NCs in NaSCN/KSCN melt, we observed colloidal solutions with *S*(q) approaching unity whenever particles were capped with S^{2-} ligands rather than treated with $NOBF_4$ stripping agent. This can be attributed to S^{2-} ions introducing a high surface charge to the NC surface and improving colloidal stability of NCs. From this perspective, S^{2-} ions acted as surfactants enabling stabilization of Pt colloid in a molten salt further highlighting the importance of chemical specificity in these systems.

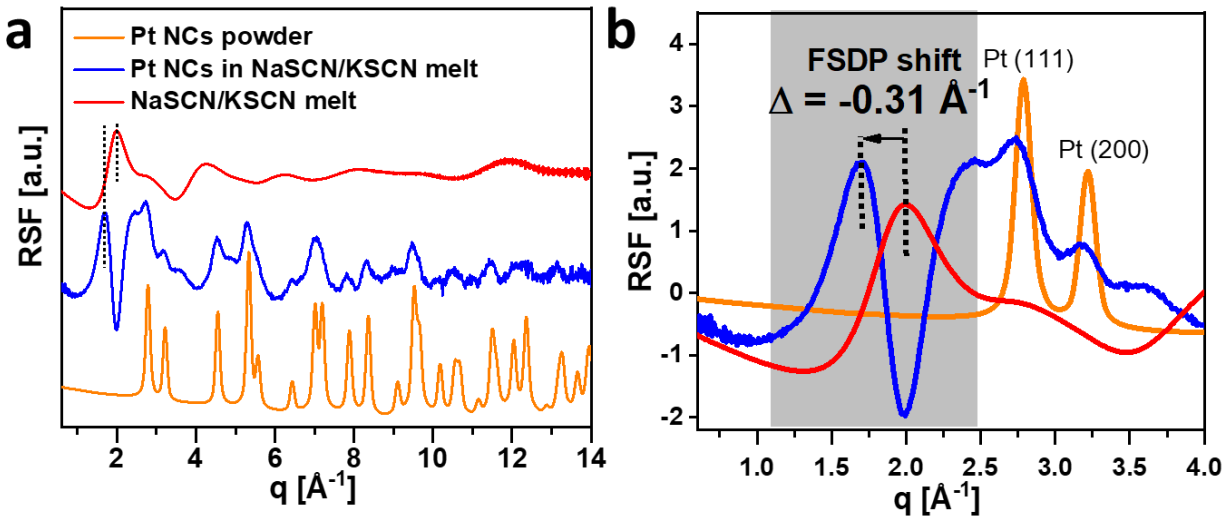

Figure S12. (a) RSF plots for Pt NCs powder, Pt NCs in NaSCN/KSCN melt (after bulk NaSCN/KSCN subtraction), and NaSCN/KSCN melt. (b) Zoom-in of the RSF plots in (a) showing the shift in the FSDP of -0.31 $Å^{-1}$ in case of Pt NCs in NaSCN/KSCN melt.

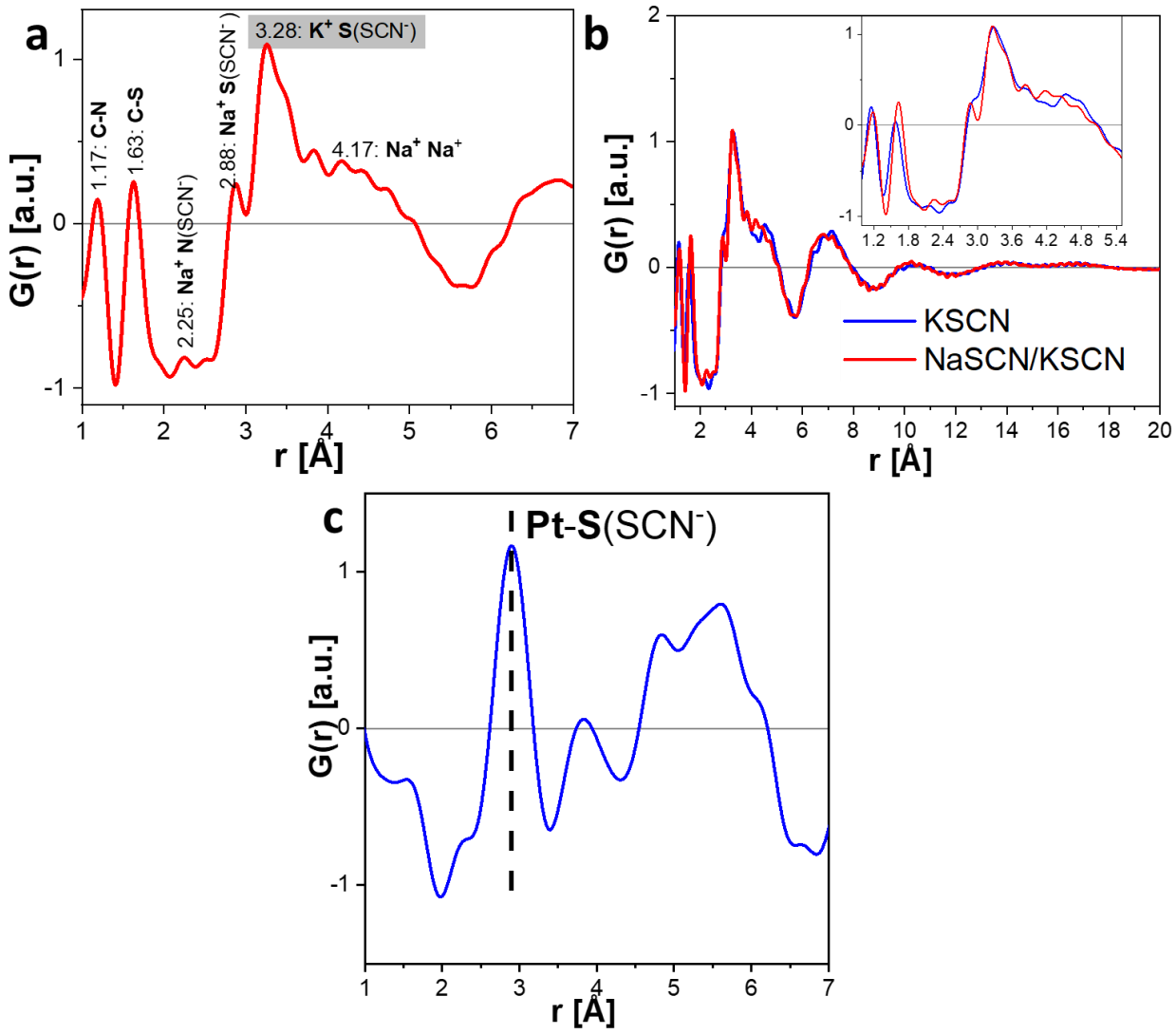

Figure S13. (a) Assignment of the sharp peaks in NaSCN/KSCN eutectic melt PDF based on the reported values. (b) Plot of the PDFs of NaSCN/KSCN eutectic melt and pure KSCN melt showing that KSCN has dominant contribution in the X-ray PDF of the eutectic mixture. (c) A sharp peak at ~2.9 Å in the dd-PDF plot for Pt NCs in NaSCN/KSCN melt likely corresponds to the distance between surface Pt atoms and S atoms of the chemisorbed SCN^- ions.

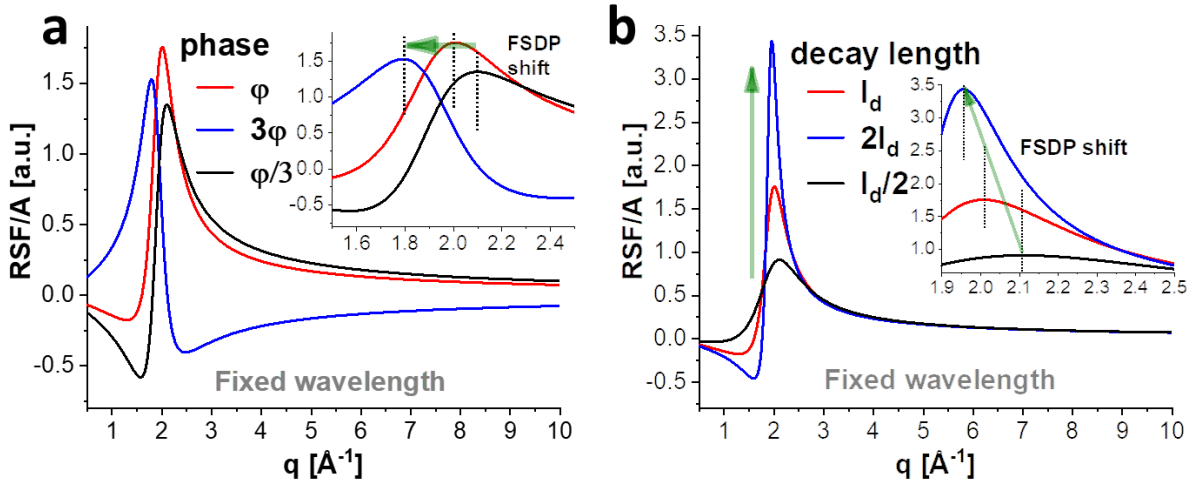

Figure S14. In order to isolate the influence of the phase (φ) and decay length (l_d) of the intermediate range order (G_{IRO}) on the FSDP, we calculated the Fourier transform of the fitting equation (eq. 5) as a function of φ and l_d. Plots (a) and (b) show dependence of the calculated *RSF(q)/A* (see eq. (6)) on the phase and decay length of $G_{IRO}(r)$ while the wavelength of oscillation (λ) is fixed. Here we use experimental parameters for NaSCN/KSCN melt with φ = 0.8, λ = 3.3 Å and l_d = 3.9 Å. (a) The change in phase primarily affects the FSDP position, where larger positive phase shift results in the low q shift of FSDP. (b) The change in the decay length primarily affects the peak FWHM where larger decay length results in sharper FSDP. These direct calculations show that the exponentially damped sinusoidal curve representing the IRO of the restructured melt can have the same λ as the bulk solvent and still exhibit FSDP with a distinct peak position and FWHM.

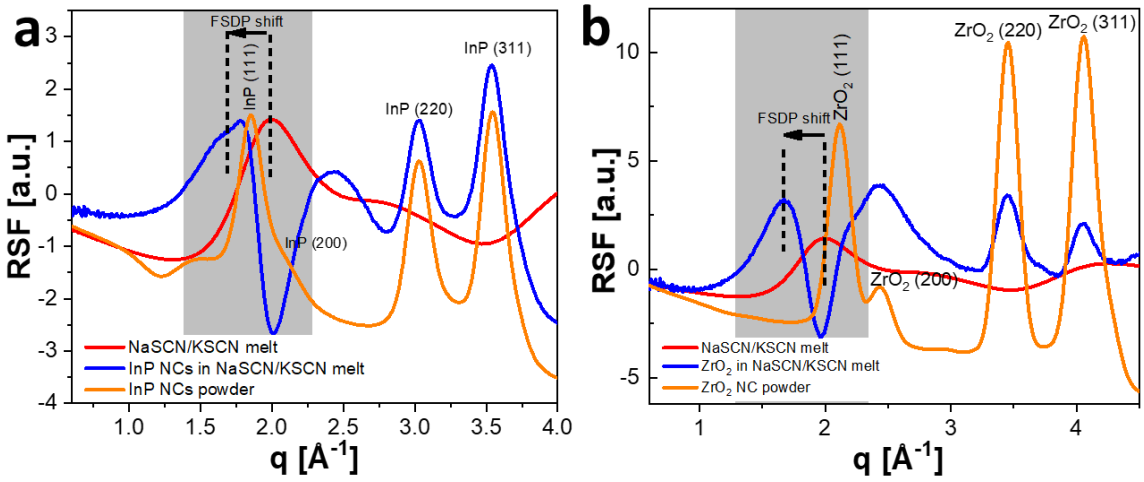

Figure S15. (a) and (b) Zoomed-in regions of the RSFs of InP and ZrO_2 NCs in NaSCN/KSCN melt respectively showing that the FSDP shift for the restructured solvent is robust in semiconductor and oxide NC.

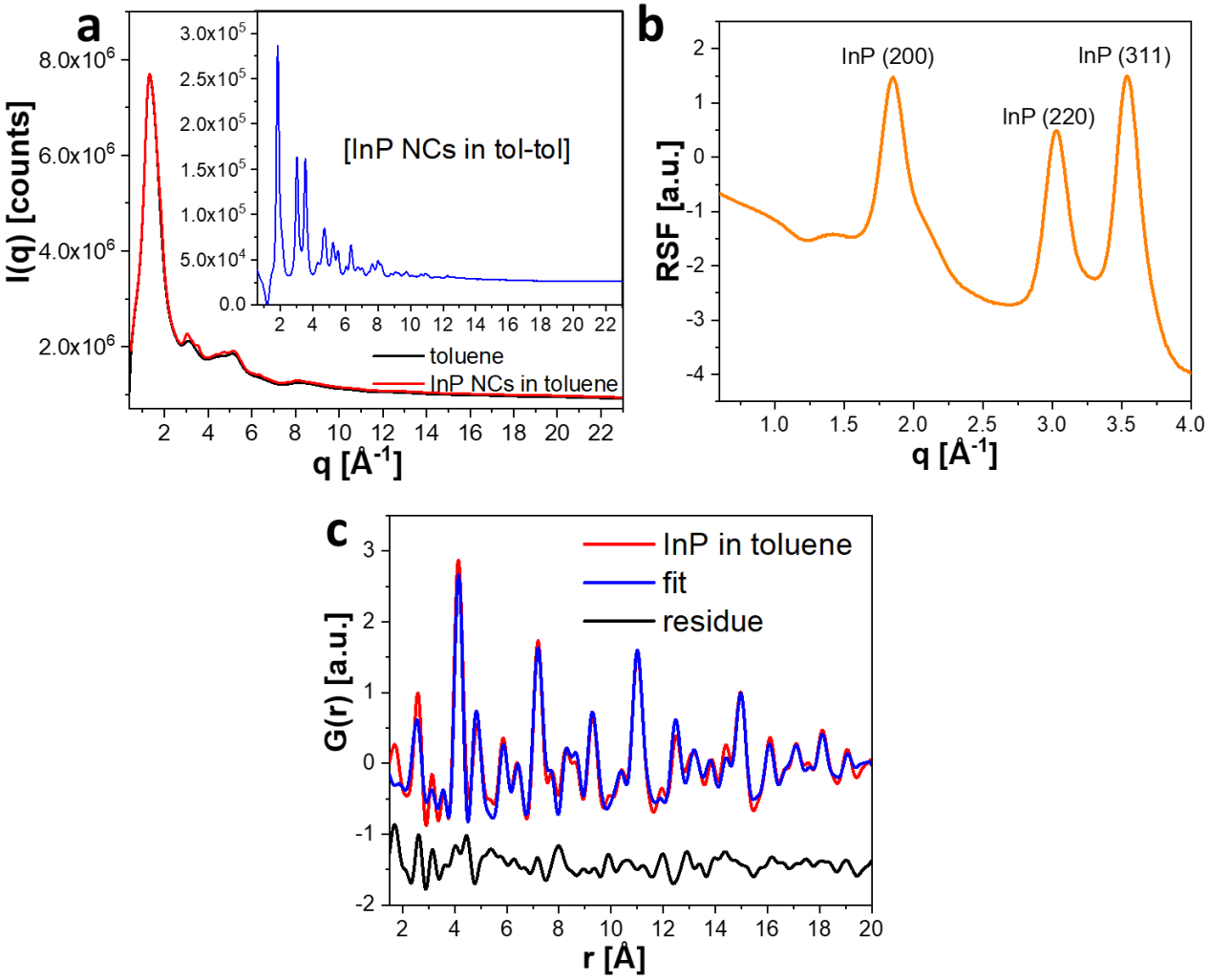

Figure S16. (a) and (b) Control experiment showing that I(q) and RSF of InP NCs in toluene after toluene background subtraction does not show any low q peaks corresponding to the restructured solvent FSDP. The resultant (c) G(r) can be fitted well as zinc-blende InP throughout the whole r region with R_w of 0.255.

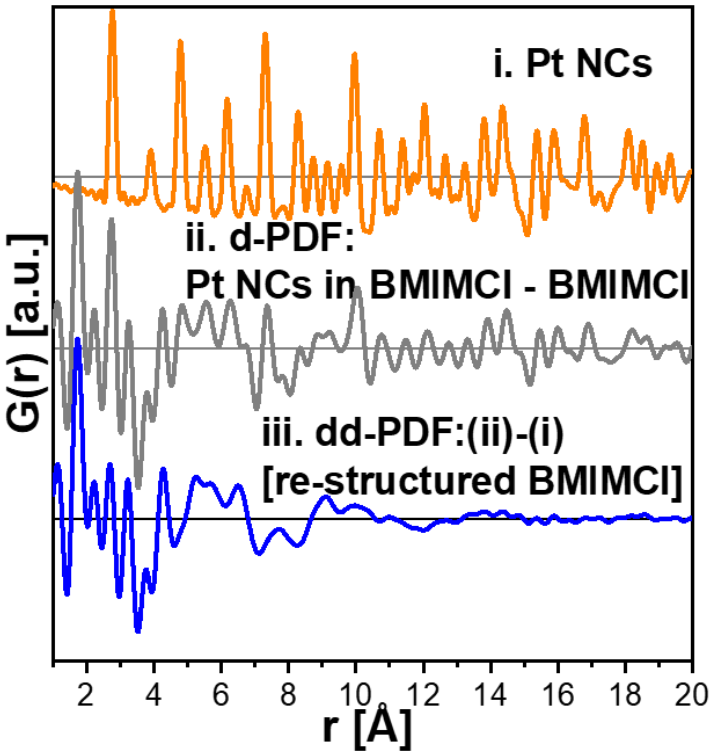

Figure S17. Experimental PDF of Pt NCs in the dry powder, d-PDF of Pt NCs in $BMIM^+Cl^-$ after the bulk liquid PDF subtraction and dd-PDF after additional subtraction of the NC contribution

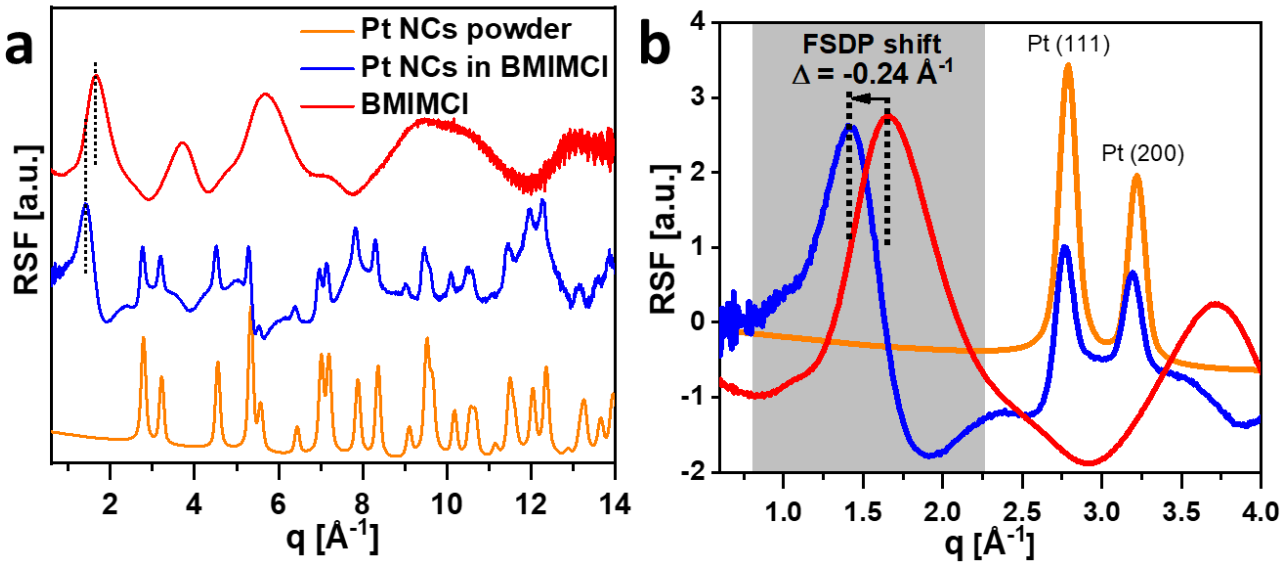

Figure S18. (a) RSF plots for Pt NCs powder, Pt NCs in $BMIM^+Cl^-$ IL (after bulk $BMIM^+Cl^-$ subtraction), and $BMIM^+Cl^-$. (b) Zoom-in of the RSF plots in (a) showing the shift in the FSDP of -0.24 $Å^{-1}$ in case of Pt NCs in $BMIM^+Cl^-$ IL.

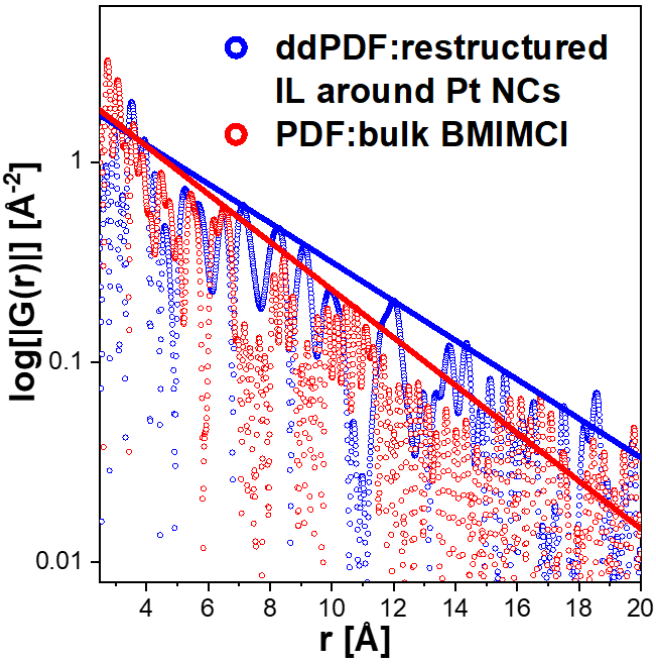

Figure S19. Logarithmic plot of the curves from panel Figure 5a showing an increase in the decay length from 3.6 Å (red curve) to 4.4 Å (blue curve) for $BMIM^{+}Cl^{-}$ IL.

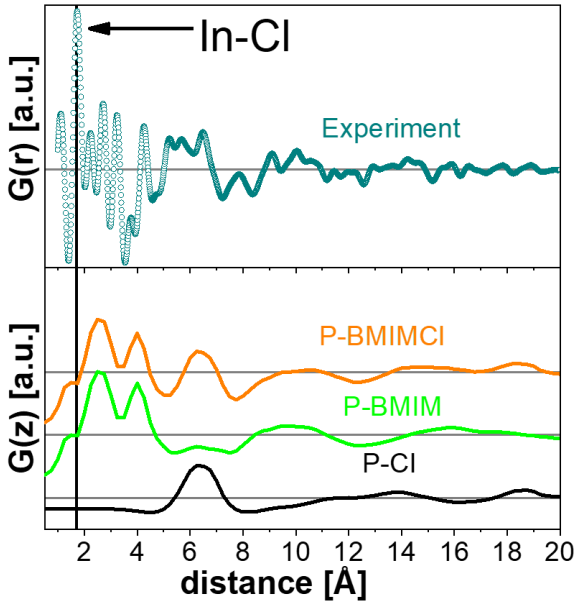

Figure S20. Comparison of the experimental PDF with the simulated linear PDF in the direction normal to P-rich NC surface, and contributions from the surface-ion correlations of P-$BMIM^{+}$, P-Cl^{-}. The most significant difference between the positive surface interaction with the solvent and the negative surface interaction with the solvent is that in the case of the In – Cl^{-} correlations, there is a very large peak for small z which doesn't appear in the P – $BMIM^{+}$ correlations.

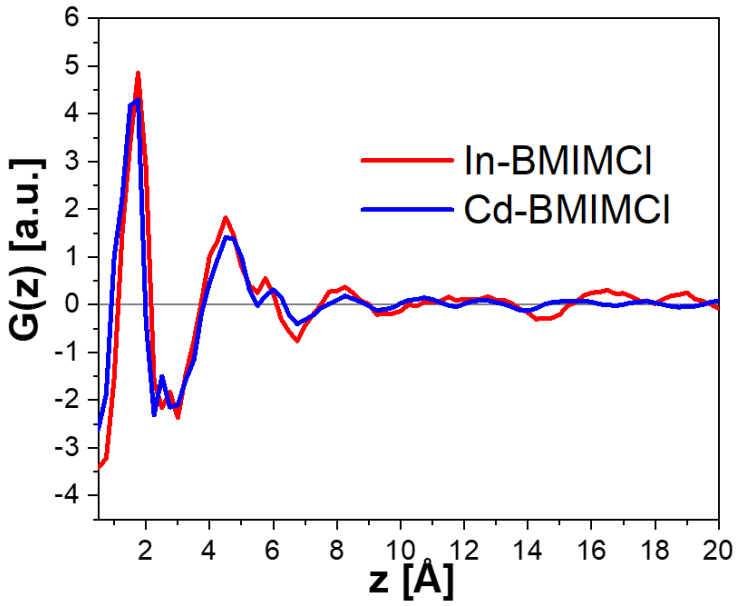

Figure S21. MD simulation results for the linear PDFs normal to In-rich InP NC and Cd-rich CdSe NC surface showing that there is little difference in the restructured $BMIM^{+}Cl^{-}$ – surface correlations.

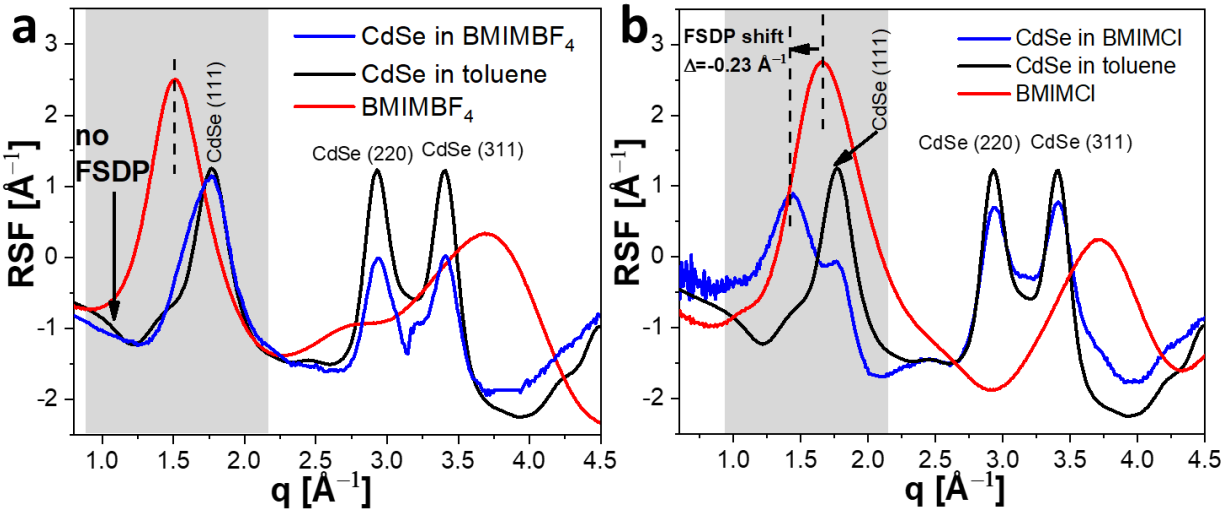

Figure S22. (a) RSF plots for CdSe NCs in toluene and $BMIM^{+}BF_4^{-}$ IL and pure $BMIM^{+}BF_4^{-}$ IL showing absence of the restructured $BMIM^{+}BF_4^{-}$ around CdSe NCs. (b) RSF plots of CdSe in toluene and $BMIM^{+}Cl^{-}$ IL and pure $BMIM^{+}Cl^{-}$ IL showing presence of the restructured $BMIM^{+}Cl^{-}$ FSDP shifted by -0.23 $Å^{-1}$ from that of the bulk IL.

Supporting references

(1) Becker, G.; Gutekunst, G.; Witthauer, C. Trimethylsilylverbindungen Der Vb-Elemente. Ii. Molekül- Und Kristallstruktur Des Tetrakis(Trimethylsilyl)-Diarsans. *Z. Anorg. Allg. Chem.* **1982,** *486*, 90-101.

(2) Kovalenko, M. V.; Scheele, M.; Talapin, D. V. Colloidal Nanocrystals with Molecular Metal Chalcogenide Surface Ligands. *Science* **2009,** *324*, 1417-1420.

(3) Ilavsky, J.; Jemian, P. R. Irena: Tool Suite for Modeling and Analysis of Small-Angle Scattering. *J. Appl. Crystallogr.* **2009,** *42*, 347-353.

(4) Beaucage, G. Approximations Leading to a Unified Exponential/Power-Law Approach to Small-Angle Scattering. *J. Appl. Crystallogr.* **1995,** *28*, 717-728.

(5) Qiu, X.; Thompson, J. W.; Billinge, S. J. L. PDFgetX2: A Gui-Driven Program to Obtain the Pair Distribution Function from X-Ray Powder Diffraction Data. *J. Appl. Crystallogr.* **2004,** *37*, 678.

(6) Zobel, M.; Neder, R. B.; Kimber, S. A. J. Universal Solvent Restructuring Induced by Colloidal Nanoparticles. *Science* **2015,** *347*, 292-294.

(7) Grünwald, M.; Zayak, A.; Neaton, J. B.; Geissler, P. L.; Rabani, E. Transferable Pair Potentials for CdS and ZnS Crystals. *J. Chem. Phys.* **2012,** *136*, 234111.

(8) Han, P.; Bester, G. Interatomic Potentials for the Vibrational Properties of III-V Semiconductor Nanostructures. *Phys. Rev. B* **2011,** *83*, 174304.

(9) Hu, Z.; Vatamanu, J.; Borodin, O.; Bedrov, D. A Molecular Dynamics Simulation Study of the Electric Double Layer and Capacitance of [BMIM][PF_6] and [BMIM][BF_4] Room Temperature Ionic Liquids near Charged Surfaces. *Phys. Chem. Chem. Phys.* **2013,** *15*, 14234-14247.

(10) Migliorati, V.; Serva, A.; Aquilanti, G.; Pascarelli, S.; D'Angelo, P. Local Order and Long Range Correlations in Imidazolium Halide Ionic Liquids: A Combined Molecular Dynamics and XAS Study. *Phys. Chem. Chem. Phys.* **2015,** *17*, 16443-16453.

(11) Pings, C. J.; Waser, J. Analysis of Scattering Data for Mixtures of Amorphous Solids or Liquids. *J. Chem. Phys.* **1968,** *48*, 3016-3018.

(12) Santos, C. S.; Annapureddy, H. V. R.; Murthy, N. S.; Kashyap, H. K.; Jr., E. W. C.; Margulis, C. J. Temperature-Dependent Structure of Methyltributylammonium Bis(Trifluoromethylsulfonyl)Amide: X Ray Scattering and Simulations. *J. Chem. Phys.* **2011,** *134*, 064501.

(13) Brown, P. J.; Fox, A. G.; Maslen, E. N.; O'Keefe, M. A.; Willis, B. T. M., International Tables for Crystallography. 2006; Vol. C, pp 554-595.

(14) Israelachvili, J. N. *Intermolecular and Surface Forces*; Academic press: London, 2011.

(15) Bergström, L. Hamaker Constants of Inorganic Materials. *Adv. Colloid Interface Sci.* **1997,** *70*, 125-169.

(16) Ordal, M. A.; Bell, R. J.; Alexander, R. W.; Long, L. L.; Querry, M. R. Optical Properties of Fourteen Metals in the Infrared and Far Infrared: Al, Co, Cu, Au, Fe, Pb, Mo, Ni, Pd, Pt, Ag, Ti, V, and W. *Appl. Opt.* **1985,** *24*, 4493-4499.

(17) Kotov, N.; Šturcová, A.; Zhigunov, A.; Raus, V.; Dybal, J. Structural Transitions of 1-Butyl-3-Methylimidazolium Chloride/Water Mixtures Studied by Raman and FTIR Spectroscopy and WAXS. *Cryst. Growth Des.* **2016,** *16*, 1958-1967.